



Article

Bowtie Nanoantenna Coupled Metal-Oxide-Silicon (p-Doped) Diode for 28.3 THz IR Rectification

Nasim Al Islam ¹ and Sangjo Choi ^{2,*} ¹ Department of Electrical, Electronic, and Computer Engineering, University of Ulsan, Ulsan 44610, Korea² School of Electronics Engineering, Kyungpook National University, Daegu 41566, Korea

* Correspondence: sangjoc@knu.ac.kr

Abstract: Low-temperature waste heat in the infrared (IR) wavelength region offers an opportunity to harvest power from waste energy and requires further investigation in order to find efficient conversion techniques. Although grating-coupled metal-oxide-semiconductor (MOS) diode devices offer efficient conversion from low and moderate-temperature thermal sources, the integration of such diodes with a nanoantenna structure has yet to be explored. We propose a bowtie nanoantenna coupled with a p-doped MOS diode for IR to direct current (DC) conversion without any bias voltage at 28.3 THz. The nanoantenna was designed and optimized to provide maximum field enhancement in a 4 nm-thick oxide layer at the resonant frequency. The device was fabricated following the complementary MOS (CMOS) fabrication process and measured in a custom DC and optical characterization setup using a 10.6 μm wavelength CO₂ laser. The results reveal two different types of devices with linear and nonlinear I-V curves having k Ω and M Ω zero-bias resistance, respectively. The linear device generates a micron-level open-circuit voltage (V_{oc}) with clear polarization dependence from the laser input, but the nonlinear case suffers from a weak noise-like signal. Finally, we analyze two types of devices using thermoelectric and tunneling effects and discuss the future direction of nanoantenna-integrated MOS devices for efficient IR harvesters.

Keywords: THz energy harvesting; MOS diode; plasmonic nanoantenna; low-temperature waste heat



Citation: Islam, N.A.; Choi, S. Bowtie Nanoantenna Coupled Metal-Oxide-Silicon (p-Doped) Diode for 28.3 THz IR Rectification. *Nanomaterials* **2022**, *12*, 3940. <https://doi.org/10.3390/nano12223940>

Academic Editors: Dana Cristea and Mihaela Kusko

Received: 17 October 2022

Accepted: 6 November 2022

Published: 9 November 2022

Publisher's Note: MDPI stays neutral with regard to jurisdictional claims in published maps and institutional affiliations.



Copyright: © 2022 by the authors. Licensee MDPI, Basel, Switzerland. This article is an open access article distributed under the terms and conditions of the Creative Commons Attribution (CC BY) license (<https://creativecommons.org/licenses/by/4.0/>).

1. Introduction

More than 50% of the heat energy emitted from transportation, industrial machinery, and various other sources in a wide range of temperatures from $-23\text{ }^{\circ}\text{C}$ to $1200\text{ }^{\circ}\text{C}$ remains unused and exists in the infrared (IR) frequency range of 20–100 THz [1,2]. For efficient global energy reuse, low-temperature waste heat must be utilized through efficient energy-harvesting techniques. Among existing methods, thermoelectric, thermophotovoltaic (TPV), and IR rectenna devices are commonly used for heat-to-energy conversion [3–5]. However, thermoelectric and TPV devices still face challenges in generating sufficient electrons above the noise level from low-temperature heat sources ($\leq 230\text{ }^{\circ}\text{C}$) for real-world applications [6,7]. Thermal rectenna-integrated tunnel diodes address this limitation by rectifying a small-signal IR wave into direct current (DC) photocurrent through direct tunneling [5]. Efficient rectification in the tunnel barrier occurs when the photonic or plasmonic resonance of the antenna overlaps with the phonon resonance of the oxide layer near epsilon near zero dispersion region [8]. Multiple research groups have demonstrated direct tunneling through metal-insulator-metal (MIM), metal-double insulator-metal (MIIM), and metal-oxide-semiconductor (MOS) tunnel diode rectifiers [5,8–14].

Recently, several studies on MIM diodes have attempted to harvest energy from a 10.6 μm (28.3 THz) IR wave source, which is equivalent to a temperature of $200\text{ }^{\circ}\text{C}$ [9,12]. When a MIM diode is illuminated by IR radiation, electrons tunnel through the oxide barrier between two metals with a high work function difference and generate a tunneling current. However, these single-insulator MIM diodes face the limitation of high resistance with low

diode asymmetry, and, therefore, require further improvement. Progress has been made to increase the diode asymmetry by introducing an extra insulator layer between two metals via MIIM diodes [10,13,15]. Energy band barrier bending at the metal-insulator interface can be controlled using two different oxide materials to create a low-resistivity path for more electrons to tunnel through. The formation of such a path to increase the tunneling current depends on the precise control of the oxide layer thickness. However, controlling these oxide layer thicknesses below 2 nm levels with sufficient precision is challenging [10,16]. As an alternative to MIM diodes, IR rectenna devices integrated with MOS tunnel diodes offer a viable solution by utilizing complementary MOS (CMOS) fabrication techniques for ease of fabrication. Previously reported unipolar MOS tunnel diodes integrated with metal gratings achieved tunneling rectification through photon-assisted tunneling between the metal and semiconductor junction [5,8,11]. Further improvement in the IR-to-DC conversion efficiency was achieved using a bipolar MOS tunnel diode [17]. The existing MOS tunnel diodes use metallic grating structures for electrodes, similar to solar cells. Since nanoantennas have been used for high field enhancement and the impedance matching with a diode to increase the output of IR harvesters, integration of the nanoantenna into a MOS diode is worth exploring [18–20].

In this paper, we propose a nanoantenna-integrated p-doped MOS diode for low-temperature IR energy-harvesting applications. We utilized a bowtie-shaped nanoantenna and optimized the dimensions for maximum field enhancement inside the oxide barrier over p-doped silicon at 10.6 μm (28.3 THz). Next, we fabricated a nanoantenna-coupled MOS diode using standard CMOS fabrication process and demonstrated its performance in DC and IR measurement setups. We examined two different types of devices with linear and nonlinear I-V curves in the same batch and analyzed their working mechanisms. Using the IR measurement setup, we measured an open-circuit voltage (V_{oc}) of both types by varying the polarization angle of the incident wave and found that the device with the nonlinear I-V curve subject to the tunneling effect failed to maintain a sufficiently high V_{oc} compared to the noise level. However, the other linear-type device exhibited a cosine-shaped micron level V_{oc} , and we analyzed that the rectification mechanism was the thermoelectric effect. Finally, we discuss future research directions for the nanoantenna-integrated MOS diode devices for efficient IR to DC rectification.

2. Design Geometry and Simulation Method

Figure 1a,b shows a simulation model and cut-view of the nanoantenna-coupled MOS diode geometry. A bowtie-shaped nanoantenna with connected arms is used as the antenna structure based on aluminum (Al). A thin layer (4 nm) of aluminum oxide (Al_2O_3) is used as an insulator layer between the metal (antenna) and a p-doped semiconductor (silicon) layer. Al_2O_3 was chosen as the oxide layer because its longitudinal optical (LO) phonon resonance is near the target wavelength, 10.6 μm . The match between the phonon and antenna resonance is intended for maximum field enhancement at the antenna from the near zero permittivity ($\epsilon \approx 0$) of the oxide material [8]. As a back reflector, a tungsten ground layer is used below the doped silicon layer to improve in-phase coupling between the incident and reflected waves near the antenna.

In this study, we used the finite element-based electromagnetic solver, ANSYS HFSS, to design and optimize the simulation model of the proposed nanoantenna-integrated MOS diode under a plane wave incident at 28.3 THz. The Al-based nanoantenna structure was optimized by placing it over the MOS diode configuration.

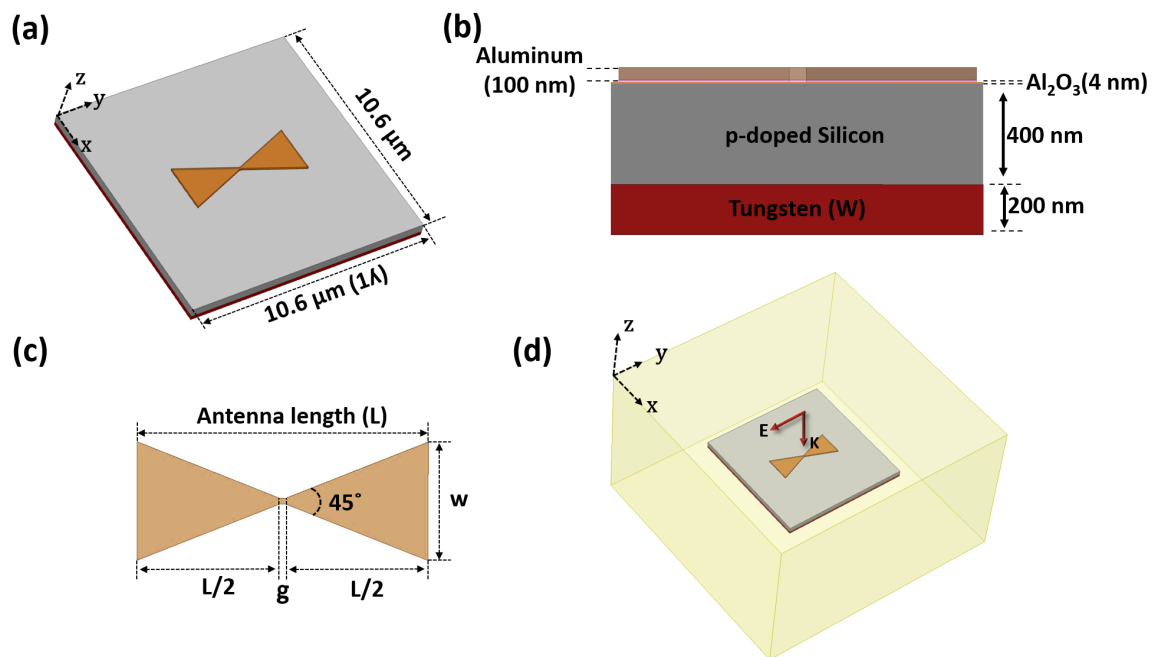


Figure 1. (a) The simulation model geometry of the nanoantenna-coupled p-doped MOS tunnel diode. (b) A cut-view of device geometry with layer thicknesses. (c) The detailed dimensions of the bowtie shaped nanoantenna. (d) The simulation environment inside a radiation boundary condition with a plane wave incident at 28.3 THz.

First, we fixed the bowtie angle to 45° and thickness to 100 nm, and varied the antenna length (L) to obtain the maximum field concentration at the antenna edges. Figure 1c shows the geometry of the antenna used for this device. Instead of proposing an air gap between the two arms of the bowtie-shaped nanoantenna, we connected two bowtie antenna arms with a square-shaped junction to maintain the DC path generated by the IR input and set the length (g) of the junction to 100 nm. In the simulation, we used a substrate size similar to the device's wavelength ($10.6 \mu\text{m}$) to reduce the computation time while maintaining antenna performance. Figure 1d shows the HFSS environment used for this simulation, where the antenna-integrated MOS diode is illuminated with a y-polarized plane wave propagating along the z-axis at 28.3 THz inside a radiation boundary. For proper modeling and simulation accuracy, the real part of relative permittivity (ϵ_{real}) and conductivity (σ) of materials in the far-IR region were calculated using Equations (1)–(3) from the Drude-model [21–23]:

$$\epsilon_{real}(\omega) = n^2 - k^2 \quad (1)$$

$$\sigma(\omega) = \epsilon_0 \times \epsilon_{im} \times \omega \quad (2)$$

$$\epsilon_{im}(\omega) = 2 \times n \times k \quad (3)$$

2.1. Antenna Length Optimization for Maximum Field Enhancement

To ensure maximum enhancement in the oxide barrier, we optimized the antenna length and width for resonance at 28.3 THz. The field enhancement is defined as the ratio between the magnitude of the electric field at the measurement point and the incident electric field (E/E_0). Here, E_0 means the y-polarized plane wave with a field intensity of 1 V/m. To calculate the field enhancement level accurately, we placed four Al_2O_3 boxes with $5 \text{ nm} \times 5 \text{ nm} \times 4 \text{ nm}$ dimensions under the four antenna edges with small mesh sizes and obtained the average field enhancement value. Figure 2a shows the averaged field enhancement inside the oxide layer below the antenna edges as a function of the antenna length (L). We found a maximum field enhancement of 29 for a $1 \mu\text{m}$ -long antenna with lower, but almost similar, values from 2–5 μm -long ones. We then selected the

shortest length of 2 μm longer than 1 μm to secure the antenna pattern more accurately during the lithography process and simultaneously reduce deposition time and expense. Figure 2b shows a cross-sectional view of the field enhancement on the top of the thin oxide layer below the 2 μm -long antenna at different resonant frequencies, 25, 28.3, and 32 THz. Maximum enhancement is observed at the antenna edges at 28.3 THz and there is a reduction of the concentrated field when moving further from the resonant frequency.

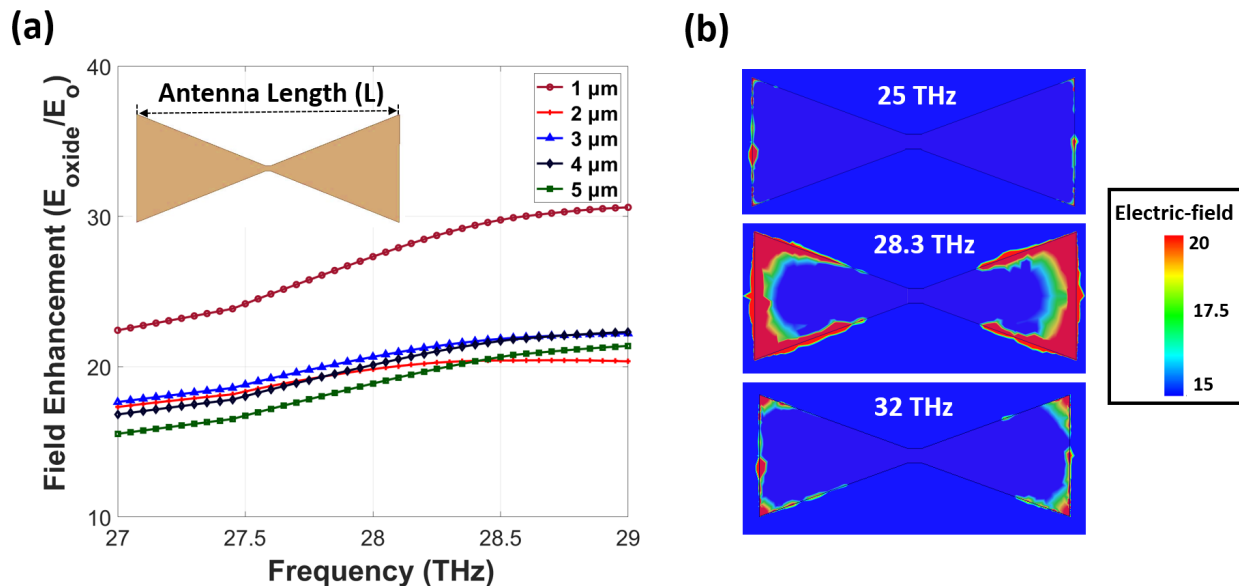


Figure 2. (a) The averaged field enhancement at 28.3 THz with variation of the antenna length at the oxide tunnel barrier below antenna edges and (b) cross-sectional view of field enhancement on the top of the oxide layer on the x-y plane for different frequencies, 25, 28.3, and 32 THz.

2.2. Connecting Wire Length Optimization

Figure 3a shows the geometry of the nanoantenna-integrated MOS diode with measurement pads. We used four different pads of size $50 \mu\text{m} \times 50 \mu\text{m}$ to connect the antenna and p-doped silicon. The overall size of a single device was $130 \mu\text{m} \times 170 \mu\text{m}$. After fixing the antenna geometry, we tuned the lengths of the connecting metallic wires (L_c) between the nanoantenna and measurement pads, which were used for mounting the probes. Here, the width of the wire was set to be 100 nm. The centers of the sides of the two antenna arms were connected to two metallic pads, as shown in Figure 3b. The measurement pads on the upper left and lower right corners were connected to the p-doped silicon layer through via connection. To ensure maximum field enhancement with a minimum effect from the connecting wire, we optimized L_c . Figure 3c shows the field enhancement variation for different values of L_c . As we varied L_c from 6 to 11 μm , we observed the maximum enhancement from a 10.6 μm (1λ)-long wire due to in-phase excitation between the two ends of the connecting wires.

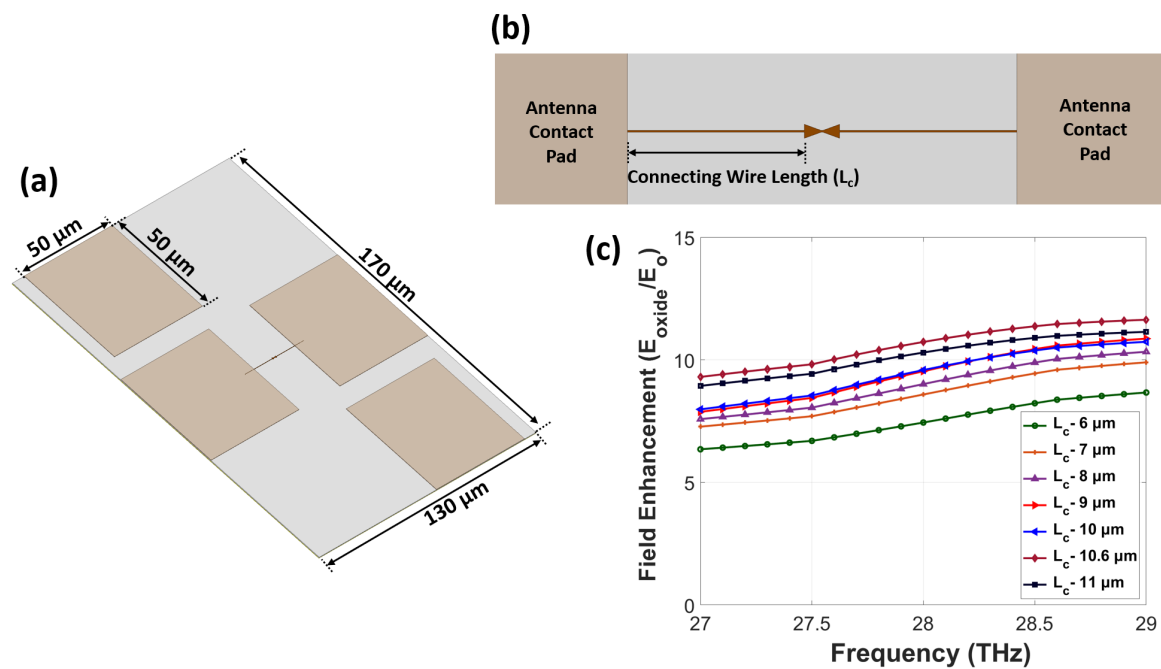


Figure 3. (a) The geometry of a nanoantenna-coupled p-doped MOS diode device with measurement pads. (b) The bowtie-shaped nanoantenna connected with the measurement pads through connecting metallic wires. (c) The frequency-dependent field enhancement versus length of the connecting wire (L_c).

3. Device Fabrication

The fabrication of the nanoantenna-coupled MOS tunnel diode was carried out by using the standard CMOS process. The process started with a p-type <100> 100 mm Si wafer. To remove the surface roughness created by native oxides over the Si wafer, buffered oxide etching (BOE) was performed. After etching, a 200 nm tungsten (W) ground layer was deposited by DC sputtering and a 400 nm poly-silicon layer was deposited over the ground layer using low pressure chemical vapor deposition (LPCVD) process. E-beam lithography was then used to pattern the p-type doping area with perfect alignment and to cover the remaining area with an e-beam resist to prevent dopant diffusion. Single-stage heavy boron implantation was then performed for p-type doping with a dose of $6.4 \times 10^{14} \text{ cm}^{-2}$ at 70 keV energy. Thermal annealing at 1000 °C for 10 s was carried out to activate and spread the dopants inside the poly-silicon layer. A very thin (4 nm) Al_2O_3 tunnel oxide layer was then deposited using atomic layer deposition (ALD) to ensure uniform distribution over the surface. Following the deposition process, the sample was coated with an e-beam resist and a bowtie-shaped nanoantenna, including connecting wires, and was patterned through an e-beam lithography lift-off process. With perfect position and alignment, a 10 nm-thick Ti adhesion layer and a 100 nm-thick Al antenna layer were deposited using the e-beam evaporation process. Before the deposition of four measurement pads, via holes with a diameter of 5 μm were etched in the p-doped silicon layer with a depth of 50 nm to ensure proper connection between the measurement pad and p-doped layer using inductively coupled plasma reactive ion etching (ICP-RIE). Finally, 50 $\mu\text{m} \times 50 \mu\text{m}$ contact pads were patterned through photolithography process and a 200 nm-thick Ti layer was deposited through the thermal evaporation. The fully processed four-terminal devices were imaged using a DM 4000M optical microscope (Leica Microsystems, Wetzlar, Germany) and a SU8220 scanning electron microscopy (SEM) (Hitachi High-Technologies, Tokyo, Japan).

Figure 4a shows the fabricated MOS device with four different measurement pads consisting of separate connections from the nanoantenna and p-doped semiconductor. The four terminals of the device offer flexibility in measuring the device in both two and four-probe measurement setups by applying a bias voltage. Among four terminals, two metallic pads were connected to the antenna arms through connecting wires for verification of

antenna connection and I-V curve measurements. The measurement pads on the upper left and bottom right were connected through via holes to the highly doped p-type silicon layer. Figure 4b,c shows a top-view SEM image of the fabricated antenna and a cross-sectional SEM image of the device, where a 2 μm -long bowtie antenna shape with the connecting wires and the precisely controlled thicknesses of the oxide, semiconductor, and ground layer can be seen.

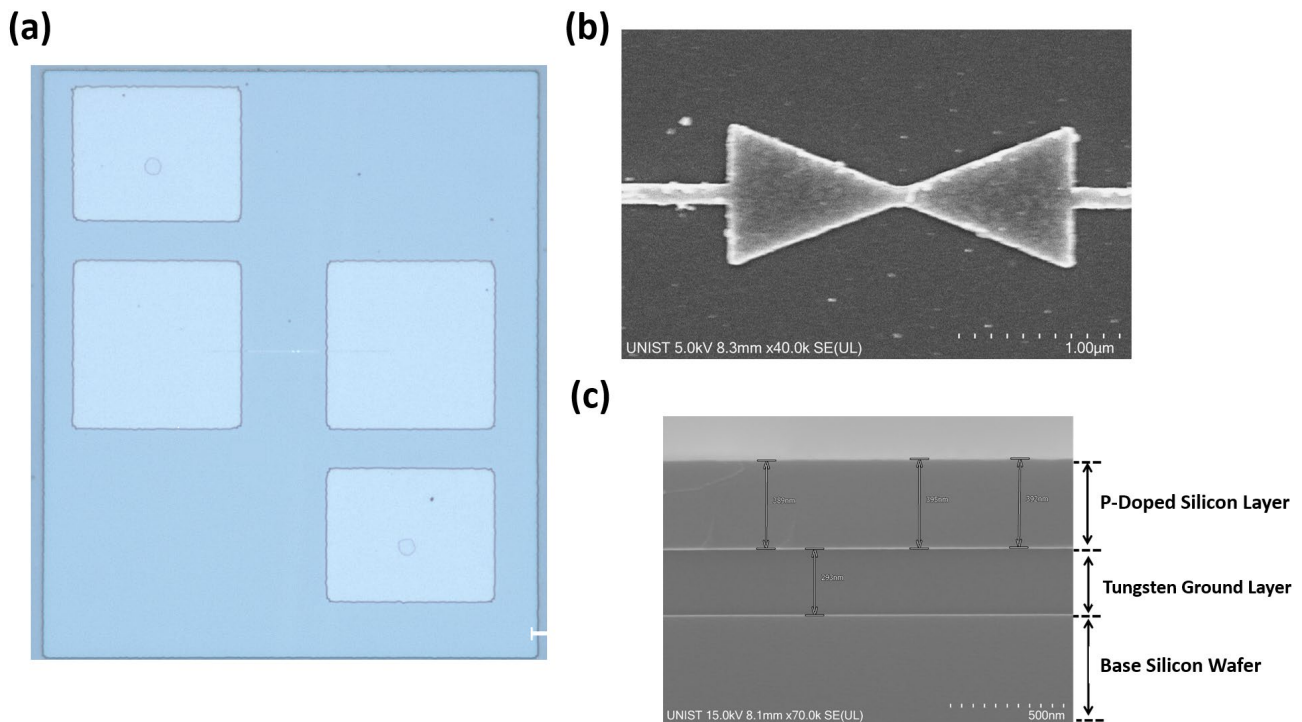


Figure 4. (a) The top view of fabricated device from an optical microscope with four measurement pads for DC and IR measurements. (b) The top view scanning electron microscopy (SEM) image of nanoantenna. (c) SEM image of cross-section of fabricated device.

4. Results and Discussion

We verified the performance of the nanoantenna-integrated MOS diode using DC and IR measurements. Figure 5 shows a schematic of the measurement setup. In the DC measurement setup, a high precision source meter KEITHLEY 2601B (Keithley Instruments, Cleveland, OH, USA) was used to accurately measure the current-voltage (I-V) curve between three different (antenna-antenna, semiconductor-semiconductor, and antenna-semiconductor) terminal pairs. The DC resistance between the terminals was calculated using the slope of the I-V curve ($R = dV/dI$). First, we verified the antenna connection of the device between the two measurement pads connected to the bowtie antenna arms. We found a low antenna resistance of approximately 80Ω for both devices, indicating a good connection between the antenna and the measurement pads. We then measured the resistance between the other two measurement pads on the upper left and lower right corners where the p-doped silicon layer is connected through the vias. Approximately 300Ω of the resistance verified a proper via connection.

Thirdly, we measured the diode's I-V curve between two measurement pads connected to the antenna and p-doped semiconductor following the method reported for MOS diodes for IR harvesting [8,11]. Since the proposed device has four measurement pads, we can measure the diode performance from any of the two pads either from the left or right side, because the device is symmetric. Here, we report all the results measured on the right-side. From the measurements, we observed two different types of devices and reported the measured I-V curves and associated differential diode resistance for both types, respectively, in Figure 6a–d. Figure 6a,b shows an almost linear I-V curve with a low diode resistance

(R_d) of 890Ω at zero bias from the first type of device. By contrast, we observed a highly nonlinear I-V curve pattern from the second type with a higher zero bias R_d of $0.6 \text{ M}\Omega$, as shown in Figure 6c,d. From now, we will call the first and second types of devices “the linear device” and “the nonlinear device” despite a slight degree of nonlinearity in the first device, for convenience. In design geometry and fabrication condition, the linear and nonlinear devices do not have any difference. Therefore, the I-V curve difference may come from the fabrication uncertainty.

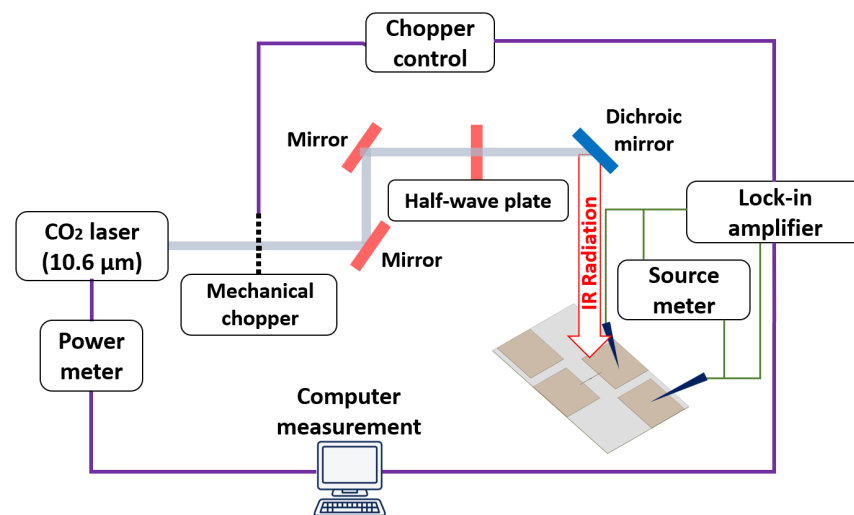


Figure 5. Schematic of the measurement setup.

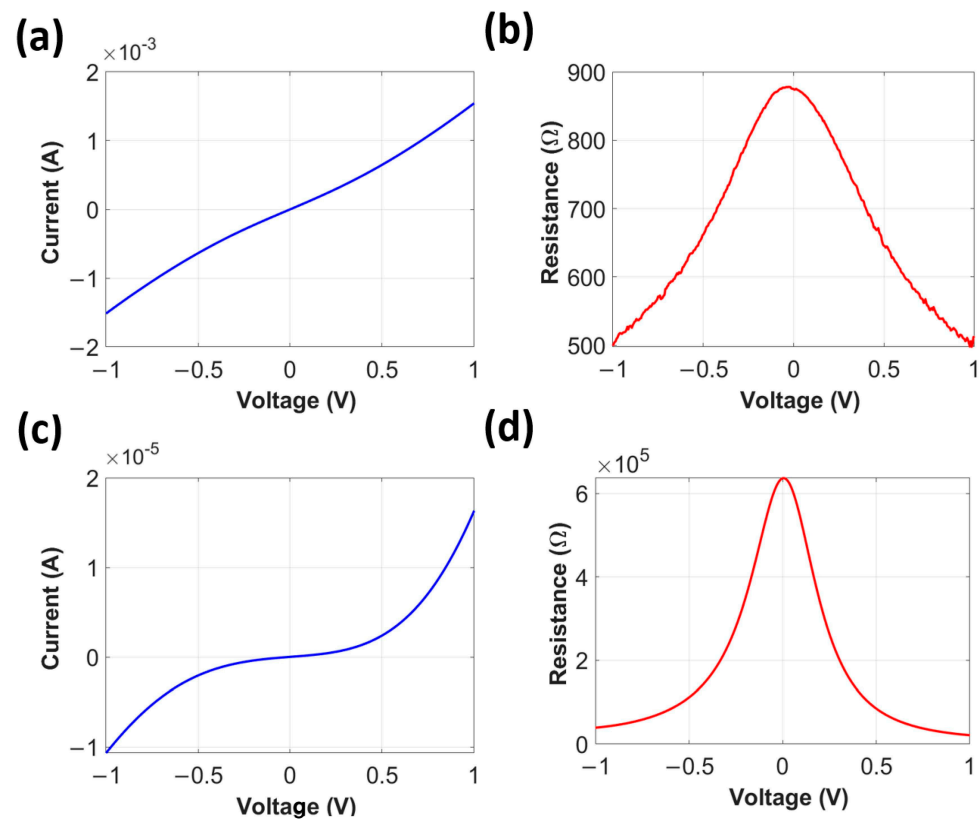


Figure 6. (a,c) Diode I-V curve and (b,d) differential diode resistance (R_d) measurement from the linear and nonlinear devices, respectively.

First, we understand that the linear device should have a dominant resistive path between the antenna and semiconductor layer due to a low zero bias R_d of 890Ω . Composi-

tion variation or defects inside the 4 nm-thin Al_2O_3 layer can be the sources of the resistive path as reported from a thermoelectric effect-based rectenna device [24]. Second, the non-linear device follows a tunnel diode-like I-V curve with a higher zero bias R_d of 0.6 $\text{M}\Omega$. We expect that in the nonlinear device, the Al_2O_3 layer works as a tunnel barrier. The $\text{M}\Omega$ range of the measured R_d is higher than the $\text{k}\Omega$ range reported for MOS devices, and the reasons may be a smaller tunneling area of a single antenna and different semiconductor properties from the proposed device compared to previously reported unipolar and bipolar MOS devices with the electrically large area of multiple gratings [11,17].

Next, the IR performance of the nanoantenna-coupled MOS tunnel diode devices was measured at 28.3 THz at zero bias condition to check the rectification ability of the devices. During the IR measurements, the devices were illuminated with a linearly polarized CO_2 laser operating at 10.6 μm (28.3 THz) with a power density of 1.77 W/cm^2 and the polarization state of the electric field (E_0) was set parallel to the antenna axis. The laser beam was modulated using a mechanical chopper with a frequency of 1 kHz and the laser beam was passed through a half-wave plate (HWP) to ensure proper polarization alignment with the antenna axis. Finally, the V_{oc} response of the device was measured using a SR830 DSP lock-in amplifier synchronized with the chopper. We measured the V_{oc} of the linear device and the value was 1.1 μV for 0° polarization angle of the incident wave. We also measured the polarization-dependent V_{oc} from the device and confirmed that a maximum V_{oc} of 1.1 μV is maintained when the polarization angles of the illuminating beam (0° and 180°) were aligned with the antenna axis. Conversely, a 90° polarization angle perpendicular to the antenna axis results in a minimum V_{oc} of 0.5 μV . The polarization-dependent nature of the linear device is shown in Figure 7, demonstrating the proper nanoantenna functionality of the device.

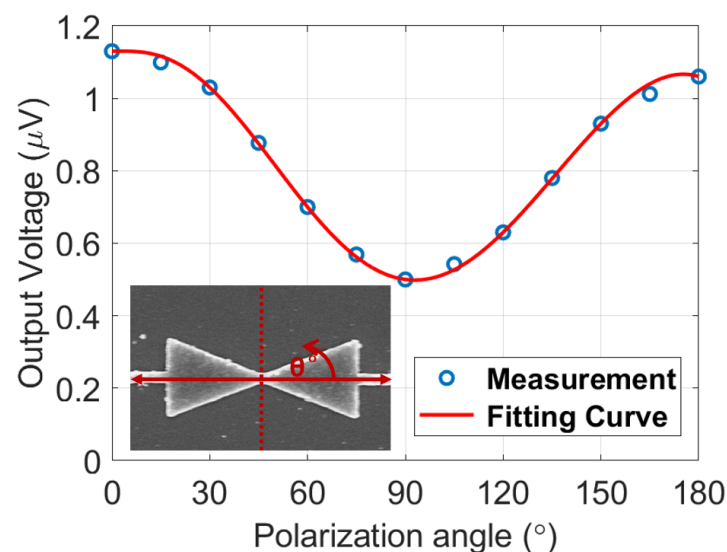


Figure 7. Polarization-dependent output voltage (V_{oc}) from the device with the linear I-V curve.

The polarization dependence and reasonably high V_{oc} level of 1.1 μV of the linear device compared to the reported nanoantenna-based MIM and thermoelectric devices are noteworthy [9,14,25,26]. We analyze that the high V_{oc} , despite the $\text{k}\Omega$ level linear resistance of the device, is only possible by thermoelectric effect based on the similar trend reported from thermoelectric IR harvesting devices [24,27]. The heated metallic antenna area on the top layer owing to the laser input and the relatively cold semiconductor layer can maintain a temperature difference (ΔT) for the thermoelectric effect. From the Seebeck coefficients of Al and p-doped Si ($S_{\text{Al}} = 3.5 \mu\text{V}/\text{K}$ and $S_{\text{p-doped Si}} = 170 \mu\text{V}/\text{K}$), the V_{oc} of 1.1 μV can be translated into a ΔT of 6.5 mK using the Equation (4) [28].

$$V_{oc} = \Delta S \times \Delta T = \left(S_{\text{p-doped Si}} - S_{\text{Al}} \right) \times \Delta T \quad (4)$$

We also note a non-negligible V_{oc} level of $0.5 \mu\text{V}$ at a 90° polarization angle and expect that it originates from the resistive connections spread inside the oxide. Although the input polarization is not aligned with the antenna axis, the heated measurement metallic pads can also contribute to the thermoelectric effect through dominant Al composition or defects inside the thin Al_2O_3 layer under the pads. For the 0° polarization angle case, the antenna edges heat up more than at other angles, and a higher V_{oc} thus can be expected.

We then measured V_{oc} from the nonlinear device and observed a noisy V_{oc} signal, as judged by the unstable fluctuation of the signal phase in the lock-in amplifier. Thus, we were unable to measure the polarization-dependent V_{oc} of the nonlinear device. The unstable noisy V_{oc} from the nonlinear device can be explained by Johnson noise, which increases with the higher resistance of the device [24,29,30]. We understand that the nonlinear device maintains a weak tunneling current level that is manifested by a $\text{M}\Omega$ zero-bias resistance, and this level is below the Johnson noise. The other V_{oc} generation from the thermoelectric effect may not be possible due to the highly resistive (insulator-like) barrier between the metal and semiconductor layers of the nonlinear device. Overall, the proposed nanoantenna integrated with the p-doped silicon showed a low tunneling-based V_{oc} and we expect that the reasons are a smaller tunneling area from the single antenna and different quality of p-doped silicon layer compared to the other grating-based MOS devices [5,11]. In future work, if the nanoantennas are designed on a more efficient bipolar MOS configuration and are constructed in a massive array, then a higher V_{oc} with a polarization-dependent trend will be possible [17].

5. Conclusions

In this study, we developed an IR to DC rectification device at 28.3 THz by using a MOS diode coupled with a bowtie-shaped nanoantenna. We optimized the nanoantenna structure on a 4 nm-thick Al_2O_3 layer and p-type silicon grounded by a metal reflector to achieve maximum field enhancement at the antenna edges. For an optimum device, the lengths of connecting wires between the antenna and the measurement pads were also optimized. Using the optimized geometric parameters of the nanoantenna, we fabricated the device by using a standard CMOS fabrication process. We then measured the diode performance by varying the bias voltage and found two different device types with linear and nonlinear I-V curves. The linear device that shows near $1 \text{ k}\Omega$ at zero bias may be enabled by composition variation or defects in the thin Al_2O_3 layer, and we expect that the device is subject to the thermoelectric effect. By contrast, the nonlinear device maintained a resistance close to $1 \text{ M}\Omega$, which could be due to weak tunneling. Optical measurements using a $10.6 \mu\text{m}$ CO_2 laser confirm a higher open-circuit voltage (V_{oc}) of $1.1 \mu\text{V}$ from the linear device with a clear polarization-dependent output. However, the nonlinear device did not produce a sufficiently high V_{oc} above the noise level. The small tunneling area of the single nanoantenna and different silicon properties compared to the electrically large grating-based MOS device may lead to weak tunneling. Despite the weak tunneling effect of the single nanoantenna, we expect that a massive array of nanoantennas with further engineering of the diode configuration can overcome the low V_{oc} limitation.

Author Contributions: Conducted numerical simulations, designed, fabricated and characterized the devices, N.A.I.; conceived the concept and supervised the research, S.C. All authors analyzed the results and wrote the manuscript. All authors have read and agreed to the published version of the manuscript.

Funding: This work was supported by the National Research Foundation of Korea (NRF) Grant funded by the Korean Government (MSIT) (No. 2020R1C1C101209912).

Data Availability Statement: Not applicable.

Acknowledgments: We thank UNIST (Ulsan National Institute of Science and Technology) Nano Fabrication Cleanroom for assistance with nanofabrication and Qbic Laser System Inc., Korea, for assistance with IR measurement setup.

Conflicts of Interest: The authors declare no conflict of interest.

References

1. Haddad, C.; Périlhon, C.; Danlos, A.; François, M.-X.; Descombes, G. Some Efficient Solutions to Recover Low and Medium Waste Heat: Competitiveness of the Thermoacoustic Technology. *Energy Procedia* **2014**, *50*, 1056–1069. [CrossRef]
2. U.S. Department of Energy. Advanced Research Projects Agency–Energy, Request for Information (RFI) DE-FOA-0001607 on Lower Grade Waste Heat Recovery. 2016. Available online: <https://viterbi.usc.edu/links/webuploads/DE-FOA-0001607%20RFI%20Lower%20Grade%20Waste%20Heat%20Recovery.pdf> (accessed on 28 September 2022).
3. Wu, Z.; Zhang, S.; Liu, Z.; Mu, E.; Hu, Z. Thermoelectric Converter: Strategies from Materials to Device Application. *Nano Energy* **2022**, *91*, 106692. [CrossRef]
4. LaPotin, A.; Schulte, K.L.; Steiner, M.A.; Buznitsky, K.; Kelsall, C.C.; Friedman, D.J.; Tervo, E.J.; France, R.M.; Young, M.R.; Rohskopf, A.; et al. Thermophotovoltaic Efficiency of 40%. *Nature* **2022**, *604*, 287–291. [CrossRef] [PubMed]
5. Shank, J.; Kadlec, E.A.; Jarecki, R.L.; Starbuck, A.; Howell, S.; Peters, D.W.; Davids, P.S. Power Generation from a Radiative Thermal Source Using a Large-Area Infrared Rectenna. *Phys. Rev. Appl.* **2018**, *9*, 054040. [CrossRef]
6. Gamel, M.M.A.; Lee, H.J.; Rashid, W.E.S.W.A.; Ker, P.J.; Yau, L.K.; Hannan, M.A.; Jamaludin, M.Z. A Review on Thermophotovoltaic Cell and Its Applications in Energy Conversion: Issues and Recommendations. *Materials* **2021**, *14*, 4944. [CrossRef]
7. Yan, Q.; Kanatzidis, M.G. High-Performance Thermoelectrics and Challenges for Practical Devices. *Nat. Mater.* **2022**, *21*, 503–513. [CrossRef]
8. Kadlec, E.A.; Jarecki, R.L.; Starbuck, A.; Peters, D.W.; Davids, P.S. Photon-Phonon-Enhanced Infrared Rectification in a Two-Dimensional Nanoantenna-Coupled Tunnel Diode. *Phys. Rev. Appl.* **2016**, *6*, 064019. [CrossRef]
9. Jayaswal, G.; Belkadi, A.; Meredov, A.; Pelz, B.; Moddel, G.; Shamim, A. Optical Rectification through an Al₂O₃ Based MIM Passive Rectenna at 28.3 THz. *Mater. Today Energy* **2018**, *7*, 1–9. [CrossRef]
10. Belkadi, A.; Weerakkody, A.; Moddel, G. Demonstration of Resonant Tunneling Effects in Metal-Double-Insulator-Metal (MI²M) Diodes. *Nat. Commun.* **2021**, *12*, 2925. [CrossRef]
11. Davids, P.S.; Jarecki, R.L.; Starbuck, A.; Burckel, D.B.; Kadlec, E.A.; Ribaudo, T.; Shaner, E.A.; Peters, D.W. Infrared Rectification in a Nanoantenna-Coupled Metal-Oxide-Semiconductor Tunnel Diode. *Nat. Nanotechnol.* **2015**, *10*, 1033–1038. [CrossRef]
12. Pelz, B.; Belkadi, A.; Moddel, G. Traveling-Wave Metal-Insulator-Metal Diodes for Infrared Rectennas. In Proceedings of the 2016 IEEE 43rd Photovoltaic Specialists Conference (PVSC), Portland, OR, USA, 5–10 June 2016; pp. 1034–1038.
13. Belkadi, A.; Weerakkody, A.; Moddel, G. Large Errors from Assuming Equivalent DC and High-Frequency Electrical Characteristics in Metal–Multiple-Insulator–Metal Diodes. *ACS Photonics* **2018**, *5*, 4776–4780. [CrossRef]
14. Pelz, B.; Moddel, G. Demonstration of Distributed Capacitance Compensation in a Metal-Insulator-Metal Infrared Rectenna Incorporating a Traveling-Wave Diode. *J. Appl. Phys.* **2019**, *125*, 234502. [CrossRef]
15. Elsharabasy, A.Y.; Bakr, M.H.; Deen, M.J. Towards an Optimal MIIM Diode for Rectennas at 10.6 μm. *Results Mater.* **2021**, *11*, 100204. [CrossRef]
16. Herner, S.B.; Belkadi, A.; Weerakkody, A.; Pelz, B.; Moddel, G. Responsivity–Resistance Relationship in MIIM Diodes. *IEEE J. Photovolt.* **2018**, *8*, 499–504. [CrossRef]
17. Davids, P.S.; Kirsch, J.; Starbuck, A.; Jarecki, R.; Shank, J.; Peters, D. Electrical Power Generation from Moderate-Temperature Radiative Thermal Sources. *Science* **2020**, *367*, 1341–1345. [CrossRef]
18. Najem, M.; Carcenac, F.; Taliercio, T.; Gonzalez-Posada, F. Aluminum Bowties for Plasmonic-Enhanced Infrared Sensing. *Adv. Opt. Mater.* **2022**, *10*, 2201025. [CrossRef]
19. Sarabandi, K.; Choi, S. Design Optimization of Bowtie Nanoantenna for High-Efficiency Thermophotovoltaics. *J. Appl. Phys.* **2013**, *114*, 214303. [CrossRef]
20. Anam, M.K.; Choi, S. Bowtie Nanoantenna Array Integrated with Artificial Impedance Surfaces for Realizing High Field Enhancement and Perfect Absorption Simultaneously. *IEEE Access* **2020**, *8*, 99858–99869. [CrossRef]
21. Ordal, M.A.; Bell, R.J.; Alexander, R.W.; Long, L.L.; Querry, M.R. Optical Properties of Au, Ni, and Pb at Submillimeter Wavelengths. *Appl. Opt.* **1987**, *26*, 744–752. [CrossRef]
22. Ordal, M.A.; Bell, R.J.; Alexander, R.W.; Newquist, L.A.; Querry, M.R. Optical Properties of Al, Fe, Ti, Ta, W, and Mo at Submillimeter Wavelengths. *Appl. Opt.* **1988**, *27*, 1203–1209. [CrossRef]
23. Kischkat, J.; Peters, S.; Gruska, B.; Semtsiv, M.; Chashnikova, M.; Klinkmüller, M.; Fedosenko, O.; Machulik, S.; Aleksandrova, A.; Monastyrskiy, G. Mid-Infrared Optical Properties of Thin Films of Aluminum Oxide, Titanium Dioxide, Silicon Dioxide, Aluminum Nitride, and Silicon Nitride. *Appl. Opt.* **2012**, *51*, 6789–6798. [CrossRef] [PubMed]
24. Bareiß, M.; Krenz, P.M.; Szakmany, G.P.; Tiwari, B.N.; Kälblein, D.; Orlov, A.O.; Bernstein, G.H.; Scarpa, G.; Fabel, B.; Zschieschang, U. Rectennas Revisited. *IEEE Trans. Nanotechnol.* **2013**, *12*, 1144–1150.
25. Szakmany, G.P.; Orlov, A.O.; Bernstein, G.H.; Porod, W. Polarization-Dependent Response of Single- and Bi-Metal Antenna-Coupled Thermopiles for Infrared Detection. *IEEE Trans. Terahertz Sci. Technol.* **2015**, *5*, 884–891. [CrossRef]
26. Szakmany, G.P.; Krenz, P.M.; Orlov, A.O.; Bernstein, G.H.; Porod, W. Antenna-Coupled Nanowire Thermocouples for Infrared Detection. *IEEE Trans. Nanotechnol.* **2012**, *12*, 163–167. [CrossRef]
27. Szakmany, G.P.; Orlov, A.O.; Bernstein, G.H.; Porod, W. Fabrication of Suspended Antenna-Coupled Nanothermocouples. *J. Vac. Sci. Technol. B Nanotechnol. Microelectron.* **2019**, *37*, 052201. [CrossRef]
28. Lide, D.R. *CRC Handbook of Chemistry and Physics*; CRC Press: Boca Raton, FL, USA, 2004; Volume 85.

-
29. Qu, J.F.; Benz, S.P.; Rogalla, H.; Tew, W.L.; White, D.R.; Zhou, K.L. Johnson Noise Thermometry. *Meas. Sci. Technol.* **2019**, *30*, 112001. [[CrossRef](#)]
 30. Bean, J.A.; Weeks, A.; Boreman, G.D. Performance Optimization of Antenna-Coupled Al/AlO_x/Pt Tunnel Diode Infrared Detectors. *IEEE J. Quantum Electron.* **2011**, *47*, 126–135. [[CrossRef](#)]